Article

Iterative Parameter Optimization for Multiple Switching Control Applied to a Precision Stage for Microfabrication

Fu-Cheng Wang [1,*], Jun-Fu Lu [1], Tien-Tung Chung [1] and Jia-Yush Yen [1,2]

1   Department of Mechanical Engineering, National Taiwan University, Taipei 10617, Taiwan;
    r07522806@ntu.edu.tw (J.-F.L.); ttchung@ntu.edu.tw (T.-T.C.); jyen@ntu.edu.tw (J.-Y.Y.)
2   Department of Mechanical Engineering, National Taiwan University of Science and Technology,
    Taipei 10617, Taiwan
*   Correspondence: fcw@ntu.edu.tw; Tel.: +886-233662680

Abstract: This paper proposes an iteration procedure to derive optimal parameters for a multiple switching control architecture. Control design is usually a compromise between various performance requirements; therefore, switching between multiple controllers that achieve a particular performance under different conditions can potentially improve the overall system behavior. In this paper, we consider a control-switching mechanism that can automatically switch controllers based on the prediction of future responses, and we develop an iteration procedure that can optimize the mechanism parameters, such as the number of controllers and the prediction horizon. We then implement the proposed mechanism in a long-stroke precision stage, and demonstrate the effectiveness of switching robust control with simulations and experiments. Lastly, we integrate the stage with a two-photon polymerization system to fabricate microlenses. The optical properties confirm that the proposed iterative parameter optimization procedure is effective in improving the performance of microfabrication employing multiple switching control.

1. Introduction

Control design is a compromise between various performance requirements. For example, controllers that provide fast transient responses tend to have large overshoots, while controllers that provide smooth responses tend to have long rise times. Therefore, switching controllers can potentially achieve better performance than can be achieved using a single controller. For instance, Solihin et al. [1] designed a fuzzy-tuned proportional integral derivative (PID) controller for a gantry crane. They updated the PID parameters according to the errors to accomplish smaller settling times and overshoots than were obtained with the original PID control. Bashash et al. [2] designed two controllers for a piezoelectric transducer (PZT) stage and switched them based on the derivatives of position errors. Qin et al. [3] designed a fuzzy adaptive PID controller for a fuel cell power plant and updated the PID parameters using fuzzy logic algorithms. Xu et al. [4] designed a fuzzy PID controller for marine vessels, where the PID coefficients were automatically adjusted by positioning accuracy. Armaghan et al. [5] designed two PID controllers and a switching logic for a magnetically driven system. Asl et al. [6] proposed a fuzzy switching control, which fused a PID controller and a linear quadratic regulator, for a unicycle robot. Rana et al. [7] applied model predictive control to improve the high-speed imaging performance of an atomic force microscope. Wang et al. [8] applied an integral control with tunable gains to a PZT stage, where the integrator eliminated steady-state errors and the varying gains provided better performance than were obtained using a fixed gain. The idea was extended in [9] by switching two robust controllers based on the prediction of future responses. Wang et al. [10] further proposed multiple-switch robust

control, which considered multiple control sequences and obtained more performance benefits than were attained with a single switching control. In this paper, we propose an iterative algorithm to tune the mechanism parameters for further improvement of system performance, because the parameters of the multiple control mechanism can significantly influence system performance and computing loads.

The stability and performance issues caused by the initial value problem in switching controls have been considered in much research. For example, Nichols et al. [11] interpolated the linear controller parameters among four H_∞ robust controllers to remove the hidden coupling terms. Yamaguchi et al. [12] proposed initial value compensation to control a hard disk driver. Because control reduction can reduce the initial value problems, Wang et al. [10] simplified high-order robust controllers into robust PID controllers that could achieve similar responses to the original controllers. In this paper, we further reduce the robust controllers to robust proportional–integral (PI) controllers, thereby reducing the computing loads in the multiple switching control mechanism.

The iterative parameter optimization procedures were then applied to a long-stroke precision positioning stage employing multiple switching control. This stage consists of a PZT stage and a motor stage, where the PZT stage achieves nanometer-level precision and the motor stage provides large displacement of up to 10 cm. The PZT stage was frequently applied for precision positioning because of its high resolution and large driving forces. However, the displacements of PZTs were usually limited. Therefore, large-travel actuators, such as linear motors, were normally integrated with the PZT stages to increase their working ranges. For instance, Wang et al. [8] integrated a motor stage and a PZT stage to achieve precision positioning for large travels. Hossain and Rahman [13] designed a triple stage, which consisted of a voice coil motor, a PZT, and a thermal flying-height control. Because the hysteretic effects of PZTs might degrade system performance, advanced control methods are usually applied to improve system performance. For example, Zhu and Rui [14] designed a PID control with an inverse generalized Bouc–Wen model to improve the precision positioning of a PZT actuator. Wang et al. [8] proposed an integral control with gain scheduling to a PZT stage. Saleem et al. [15] applied a Bouc–Wen model and particle swarm optimization (PSO) to compensate for the hysteretic characteristics. Gan and Zhang [16] developed a generalized Bouc–Wen model to characterize the rate-dependent hysteresis of PZTs. Fang et al. [17] developed a modified Bouc–Wen model and designed a fuzzy PID control with an inverse model feedforward compensator for a PZT stage. Wang et al. [10] proposed an automatic switching control for a PZT stage. Zhang et al. [18] designed an autonomous switching control to suppress the vibration of a double-beam system employing piezoelectric shunt damping. In this paper, we designed robust controllers for the PZT stage and optimized the switching parameters via the proposed iterative procedures. We then applied similar approaches to the motor stage. Because the motor stage model is a first-order type, its switching control can be further simplified to gain scheduling with feedforward control to reduce the computing loads. The two stages were then combined to demonstrate the system's capacity for long-stroke precision positioning. Lastly, we integrated the combined stage with a two-photon polymerization (TPP) system, and showed the benefits of multiple switching control employing iterative parameter optimization in microfabrication.

The rest of this paper is arranged as follows: Section 2 introduces the multiple switching control structure and proposes an iterative procedure to optimize the structure parameters. Section 3 applies the iterative parameter optimization method to a large-stroke precision stage. The simulation and experimental results demonstrate the effectiveness of the proposed iterative parameter tuning. We further integrate the stage with a TPP system to fabricate microlenses and demonstrate the effectiveness of the proposed iterative parameter optimization in microfabrication. Lastly, we draw conclusions in Section 4.

2. Multiple Switching Control with Iterative Parameter Optimization

The multiple switching control architecture is shown in Figure 1, consisting of a feedback control loop and a response predictor. The former implements the selected controller to the system, while the latter picks the best controller that provides the optimal system responses among all potential control sequences. We propose an iterative algorithm to optimize the structure parameters, such as the number of controllers, the prediction horizon, and the switching steps.
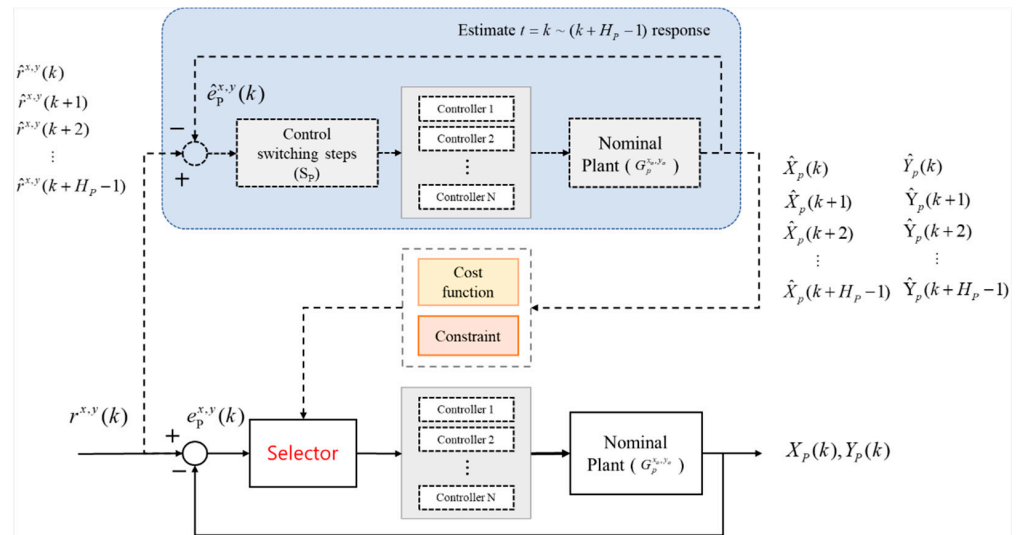

Figure 1. The multiple switching control structure.

Because control design is usually a compromise between various performance requirements, we can combine the merits of different controllers by switching them at appropriate instances. For example, consider a standard second-order system $G(s) = \omega_n^2 / (s^2 + 2\xi\omega_n s + \omega_n^2)$ with $\xi = 1$ and $\omega_n = 6$; the controller design is a compromise between various specifications, such as the rise time, the overshoot, and the steady-state error. For instance, a controller $C_1(s) = 3/s$ can provide a short rise time with zero steady-state error, but with a large overshoot, while a controller $C_2(s) = 0.8/s$ can achieve small overshoot and zero steady-state error, but with a long rise time. Therefore, we can combine the advantages of these two controllers by switching them at the right moments. For example, we can define the system cost as follows:

$$J = \sqrt{\frac{1}{H_P} \cdot \sum_{k}^{k+H_p} (r(k) - y(k))^2} \tag{1}$$

where k is the current step and H_p is the future horizon. That is, the predictor calculates the future system responses from step k to step $k + H_p$, and the corresponding cost J, by all potential control sequences. Then, the optimal control sequence that minimizes J is selected to control the system. For example, we set $H_p = 40$ and derive the system response, as shown in Figure 2, where the switching control achieves short rising time, small overshoot, and small steady-state error simultaneously.
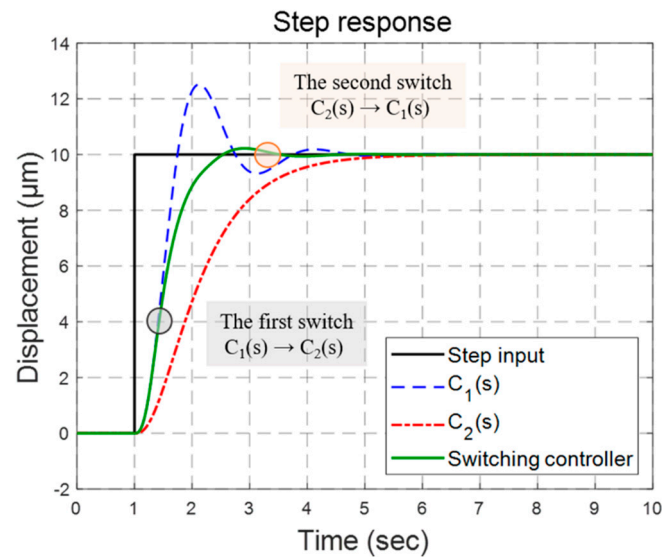
Figure 2. Response improvement by the switching control.

Because the performance of the switching control structure can be significantly influenced by the structure parameters, we propose a method to tune these parameters. As shown in Figure 1, the response predictor estimates future system responses by all possible control sequences, and selects the optimal control sequence that minimizes certain system costs. Suppose that there are N controllers, and the number of controller switching steps is S_p; the number of possible control sequences is then N^{S_P}. For instance, suppose that two controllers—C1 and C2 (i.e., $N = 2$)—have two switching steps (i.e., $S_p = 2$); there will be $2^2 = 4$ possible control sequences, as follows: (C1, C1, C1, ... , C1), (C1, C2, C2, ... , C2), (C2, C1, C1, ... , C1), (C2, C2, C2, ... , C2). Therefore, the predictor needs to calculate the system responses employing these four control sequences, and then choose the optimal control sequence that minimizes certain performance indices.

Although the control parameters can significantly influence the system performance, simultaneous optimization of these parameters is impractical because of the hardware computing loads. For example, the predictor needs to estimate the future system responses in the next H_p steps with N^{S_P} control sequences. Therefore, we propose an iterative method that can tune these parameters one by one at each iteration until they converge. For example, suppose that we have three structure parameters (N, H_P, S_P), where N is the number of controllers, H_p is the prediction horizon, and S_p is the number of switching steps. The proposed iteration procedures are illustrated as follows (see Figure 3):

1. Set the default parameters (N, H_P, S_P);
2. Apply (N, H_P, S_P) to derive an optimized N, labelled as N^{opt}, which can improve system performance without exceeding hardware computing limits;
3. Apply (N^{opt}, H_P, S_P) to derive an optimized H_p, labelled as H_P^{opt}, which can improve system performance without exceeding hardware computing limits;
4. Apply (N^{opt}, H_P^{opt}, S_P) to derive an optimized S_p, labelled as S_P^{opt}, which can improve system performance without exceeding hardware computing limits;
5. If (N^{opt}, H_P^{opt}, S_P^{opt}) = (N, H_P, S_P), then the iteration is terminated, and the optimal parameters (N^{opt}, H_P^{opt}, S_P^{opt}) can be implemented by the multiple control structure. Otherwise, set (N, H_P, S_P) = (N^{opt}, H_P^{opt}, S_P^{opt}) and return to step 1.
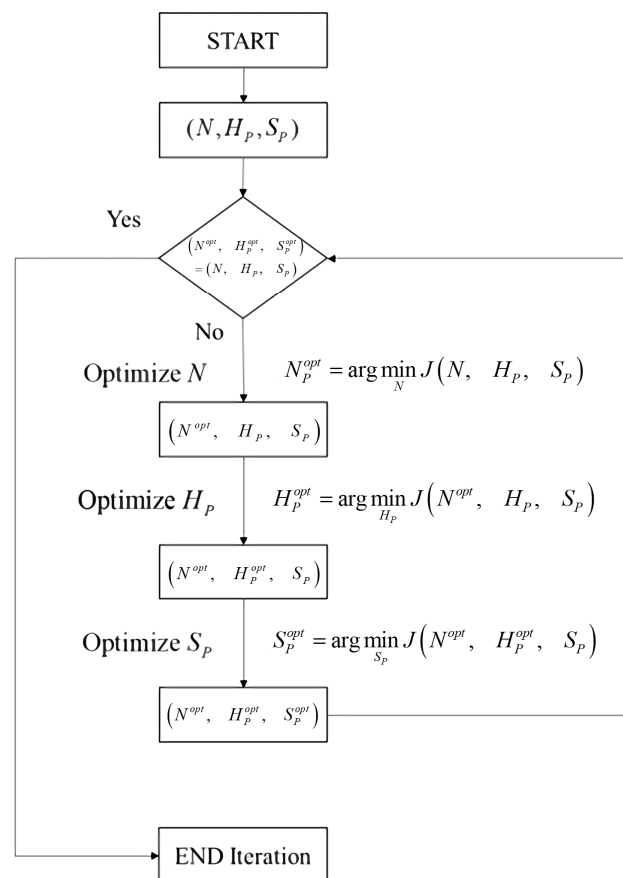
Figure 3. The procedures of iterative parameter tuning.

3. Iterative Parameter Optimization for the Long-Stroke Precision Stage Employing Multiple Switching Control

This section applies the proposed iterative parameter tuning method to the long-stroke precision stage employing multiple switching control. This stage consists of a PZT stage and a motor stage, as illustrated in Figure 4. The specifications of the stage are illustrated in Table 1. We apply the switching control mechanism to both stages, and integrate them for simulations and experiments.

Table 1. Specifications of the long-stroke precision stage.

P-517.RCD PZT Stage [19]	
Active axis	x, y
Maximum stroke	−50 to 50 μm
Mass	1.4 kg
Resolution	1 nm
SVR/150/3 amplifier [20]	
Output voltage range	−30 to 150 V
Max gain	30 (tunable)
ALS-510-H2 P stepper [21]	
Active axis	x, y
Maximum stroke	100 mm
Resolution	0.1 μm
Maximum loading	40 kgf
Maximum command	80,000 pulse/sec
ALV-104-HP stepper [22]	
Active axis	z
Maximum stroke	40 mm
Resolution	0.1 μm
Maximum loading	10 kgf
Maximum command	40,000 pulse/sec
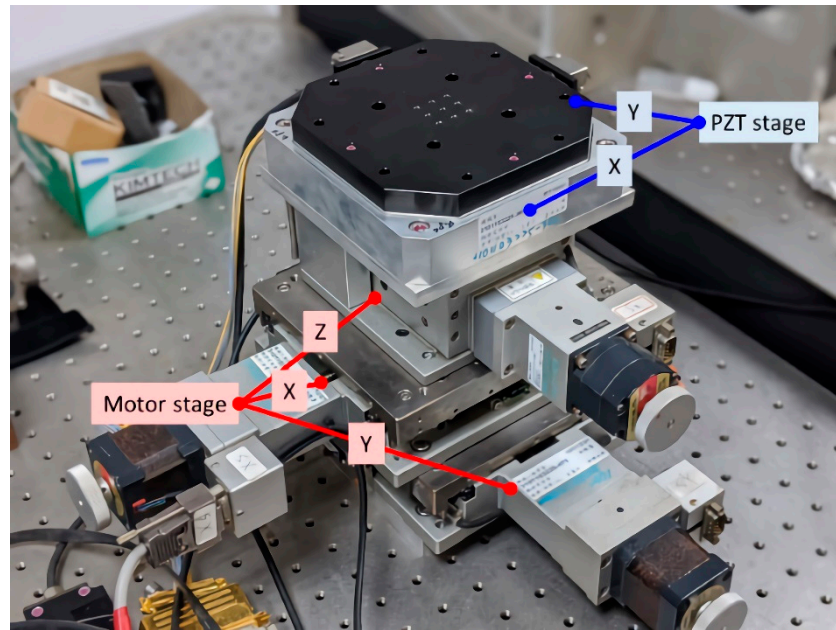
Figure 4. The long-stroke precision stage.

3.1. Multiple Switching Control for the PZT Stage

The PZT stage [19] has a travel range of 100 μm and is equipped with an encoder with a resolution of 1.22 nm. We applied PCI-6221 and PCI-6229 data acquisition (DAQ) cards [23] to measure the stage displacements, and to transmit the control signals within ±5 V. Because the operation voltage of the PZT was −20 to 120 V, we used an SVR/150/3 amplifier [20] to magnify the voltage signals 10-fold and offset 50 V to control the stage displacements between 0 and 100 μm.

The system model was derived from the following experiments: we applied a swept sinusoidal voltage signal V_P and measured the stage displacements X_P from the encoder. Given the system variation and uncertainties during operations, we repeated the procedures 10 times and obtained the following transfer functions:

$$G_P^i(s) = T_{v_P \rightarrow X_P}, \ \ i = 1, 2, \ldots, 10 \tag{2}$$

A nominal plant was selected for the controller design. We assume that a nominal plant G_P^o has the following left coprime factorization [24]:

$$G_P^o = \widetilde{M}^{-1}\widetilde{N}, \tag{3}$$

where $\widetilde{M}, \widetilde{N} \in RH_\infty$ and $\widetilde{M}\widetilde{M}* + \widetilde{N}\widetilde{N}* = I$. Suppose that a perturbed plant G_P^Δ can be represented as:

$$G_P^\Delta = \left(\widetilde{M} + \Delta_{\widetilde{M}}\right)^{-1}\left(\widetilde{N} + \Delta_{\widetilde{N}}\right), \tag{4}$$

in which $\Delta_{\widetilde{M}}, \Delta_{\widetilde{N}} \in RH_\infty$. The gap between the nominal plant G_P^o and the perturbed plant G_P^Δ is defined as in [25]. The smallest value of $\left\|\left[\Delta_{\widetilde{M}}\Delta_{\widetilde{N}}\right]\right\|_\infty$ that perturbs G_P^o into G_P^Δ is denoted as $\delta(G_P^o, G_P^\Delta)$. Based on the gap analyses, the following G_P^1 was selected as the nominal plant G_P^o, because it minimized the maximum gaps between models:

$$
\begin{aligned}
G_P^o &= \arg\left\{\varepsilon = \min_{G_P^o}\max_{G_P^i}\delta_g(G_P^0, G_P^i)\right\}, \ \forall i \\
&= G_P^1(s) = \frac{1517s^3 + 1.75\cdot10^5s^2 + 6.053\cdot10^8s + 1.778\cdot10^{10}}{s^4 + 292.6s^3 + 4.142\cdot10^5s^2 + 8.282\cdot10^7s + 2.064\cdot10^9}
\end{aligned}
\tag{5}
$$

We designed the following three robust loop-shaping controllers [26] for G_P^o:

$$C_F = \frac{67.3s^6 + 4.19 \times 10^4 s^5 + 1.53 \times 10^{10} s^3 + 2.73 \times 10^{12} s^2 + 1.97 \times 10^{14} s + 3.79 \times 10^{15}}{s^7 + 923s^6 + 6.50 \times 10^5 s^5 + 3.59 \times 10^8 s^4 + 7.48 \times 10^{10} s^3 + 5.45 \times 10^{12} s^2 + 1.04 \times 10^{14} s}$$

$$C_M = \frac{34.8s^6 + 1.81 \times 10^4 s^5 + 1.67 \times 10^7 s^4 + 6.21 \times 10^9 s^3 + 7.40 \times 10^{11} s^2 + 3.26 \times 10^{13} s + 4.63 \times 10^{14}}{s^7 + 883.2s^6 + 6.19 \times 10^5 s^5 + 3.36 \times 10^8 s^4 + 6.35 \times 10^{10} s^3 + 3.60 \times 10^{12} s^2 + 5.92 \times 10^{13} s} \quad (6)$$

$$C_S = \frac{12.1s^6 + 5912s^5 + 5.77 \times 10^6 s^4 + 2.00 \times 10^9 s^3 + 2.42 \times 10^{11} s^2 + 1.07 \times 10^{13} s + 1.52 \times 10^{14}}{s^7 + 697s^6 + 5.49 \times 10^5 s^5 + 2.56 \times 10^8 s^4 + 4.20 \times 10^{10} s^3 + 2.34 \times 10^{12} s^2 + 3.87 \times 10^{13} s}$$

where C_F, C_M, and C_S provide fast, intermediate, and smooth responses, respectively, for the PZT stage. The control design processes are illustrated in Appendix A, in which the stability margins of all controllers are greater than the system gap $\left\| \left[\Delta_{\tilde{M}} \Delta_{\tilde{N}} \right] \right\|_\infty$; therefore, internal stability can be guaranteed during operation.

Because the designed robust controllers are seventh-order controllers, this might increase the computing loads and cause initial value problems. Therefore, we also apply the PSO algorithms [27] to approximate these controllers as the following robust PI controllers:

$$\overline{C}_F = 0.05 + \frac{36.97}{s}, \ \overline{C}_M = 0.08 + \frac{8.01}{s}, \ \overline{C}_S = 0.05 + \frac{3.94}{s} \quad (7)$$

The design of the robust PI controllers is shown in Appendix B. The system responses by these controllers are illustrated in Figure 5 and Table 2, where the robust PI controllers provide system responses similar to those of the high-order robust controllers, but with much simpler forms. That is, the fast controllers $\overline{C}_F$ provide faster responses (i.e., shorter rise time and settling time), but with larger overshoots than are achieved with the other controllers. Conversely, the smooth controllers $\overline{C}_S$ give smooth responses (i.e., without overshoot), but with larger rise times and settling times than are seen for the other controllers. The behaviors of the intermediate controllers $\overline{C}_M$ fall between the fast controllers and the smooth controllers. We further add an extra controller $\overline{C}_4 = 0.07 + 23.01/s$ with characteristics between $\overline{C}_F$ and $\overline{C}_M$. We will demonstrate the possibility of achieving the merits of these controllers simultaneously with a switching control employing the iterative optimization procedures.
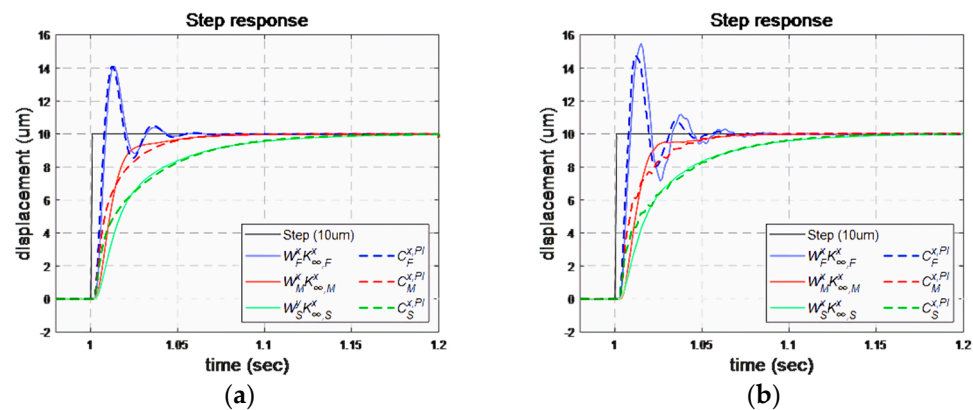
Figure 5. Comparison of the standard robust controllers and the robust PI controller: (**a**) simulation; (**b**) experimental results.

We applied the iteration procedures (see Figure 3) to derive the optimal parameters for the switching control mechanism. The processes are shown in Appendix C, where the optimal parameters were $\left(N^{opt} = 3, \ H_P^{opt} = 20, \ S_P^{opt} = 2 \right)$. Therefore, we implemented these parameters in the PZT stage employing the multiple control structure, and we illustrate the system responses in Figure 6. At $t = 1$ s, the stage began to track a step command of 10 μm with the fast controller $\overline{C}_F$. Based on the response prediction, the switching mechanism switched the controller to $\overline{C}_S$ at $t = 1.003$ s, and to $\overline{C}_M$ at $t = 1.004$ s. Finally, the fast controller $\overline{C}_F$ was chosen at $t = 1.02$ s to track the step command. As shown

in Figure 6, the switching control combined the merits of these controllers to achieve a fast and smooth response.

Table 2. Statistical comparison of the controllers.

		Robust Controller			Robust PI Controller		
		C_F	C_M	C_S	$\overline{C}_F$	$\overline{C}_M$	$\overline{C}_S$
Sim.	Rise time (sec)	0.0043	0.0171	0.0622	0.0051	0.0327	0.0692
	Settling time (sec)	1.0415	1.0612	1.1331	1.0563	1.0654	1.1283
	Overshoot (%)	41.1600	0	0	39.2792	0.0101	0
	RMSE (µm)	1.6834	2.0511	2.6434	1.6863	1.8733	2.5951
Exp.	Rise time (sec)	0.0043	0.0158	0.0622	0.0038	0.0287	0.0654
	Settling time (sec)	1.0647	1.0579	1.1269	1.0495	1.0574	1.1183
	Overshoot (%)	54.8200	0.1100	0	47.4300	0.2100	0.0500
	RMSE (µm)	1.8872	2.1419	2.7021	1.6934	1.9034	2.4406

Sim.: simulation; Exp.: experiments.
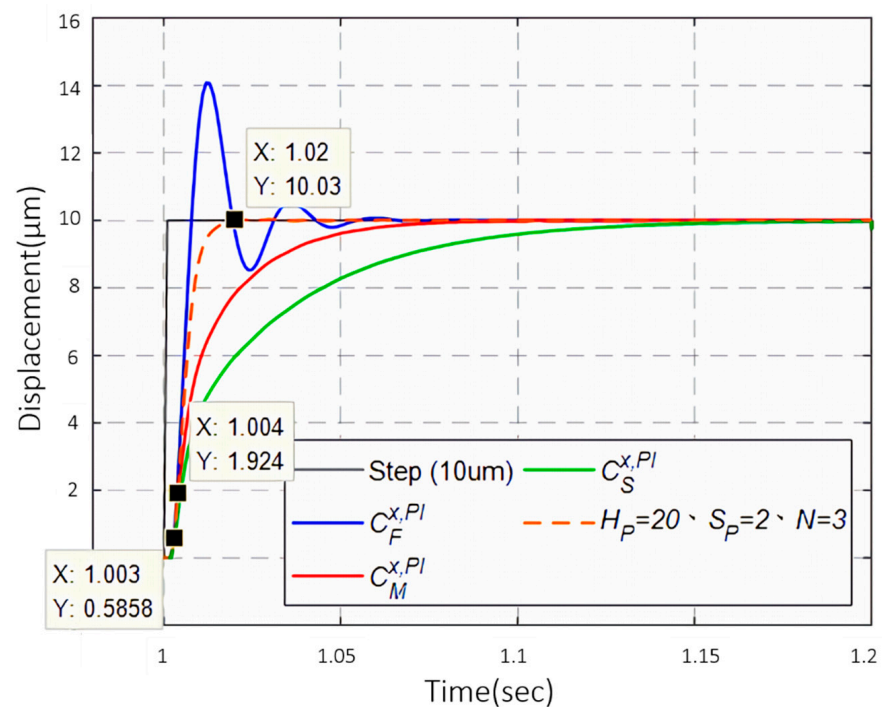
Figure 6. Step response of PZT stage employing the optimal switching control.

3.2. Switching Control for the Motor Stage

The motor stage [21,22] has a travel range of 10 cm, and is equipped with an encoder with a resolution of 0.1 µm. Similarly, we derived its transfer functions from experiments, and selected the nominal plant, as follows:

$$G_M^o = \frac{0.1}{s} \tag{8}$$

for control design. Because G_M^o is first-order, we only need to apply a zero-order control K_P to achieve arbitrary pole placement. Therefore, we designed a gain-scheduling control with command feedforward, as shown in Figure 7, for the motor stage.
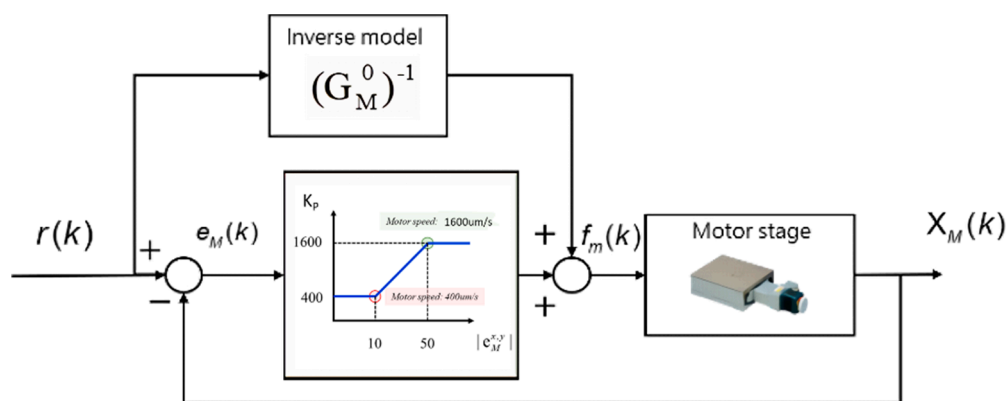
Figure 7. Gain-scheduling control with command feedforward for the motor stage.

The gain scheduling control is a stepless switching control based on tracking errors, while the command feedforward can reduce tracking errors for varying inputs, such as ramp or sinusoidal inputs. The gain-scheduling control can be represented as $C(s) = K_p$, where K_p is adjusted by the following equation:

$$K_P = \begin{cases} 1600, \text{ if } |e_M| \geq 50\mu m \\ 30 \cdot |e_M| + 100, \text{ if } 10 < |e_M| < 50\mu m \\ 400, \text{ if } |e_M| \leq 10\mu m \end{cases} \tag{9}$$

We applied the motor stage for tracking the ramp and sinusoidal inputs. The results are shown in Figure 8 and Table 3. First, Figure 8a,b shows the tracking responses to the ramps of 100 μm/s and 500 μm/s, respectively. The gain-scheduling control was set as $K_p = 400$, because the tracking errors were less than 10 μm. Compared to the control used in [9], the RMSE was decreased from 2.4797 μm to 0.2238 μm for the ramp of 100 μm/s, and from 8.7794 μm to 0.7851 μm for the ramp of 500 μm/s. Second, the tracking responses for sinusoidal inputs of 0.1 Hz and 1 Hz are shown in Figure 8c,d, respectively. Similarly, the gain-scheduling control was set as $K_p = 400$, because the tracking errors were less than 10 μm. Compared to the control used in [9], the RMSE was reduced from 0.5609 μm to 0.1355 μm for $r(t) = \sin(0.2\pi t)$, and from 5.5460 μm to 0.4161 μm for $r(t) = \sin(2\pi t)$.

Table 3. Tracking performance of the motor stage.

	Inputs	Ramp		Sinusoidal	
	Sizes	100 μm/s	500 μm/s	0.1 Hz	1 Hz
Sim.	Phase lag (°)	-	-	0	0
	Maximum error (μm)	0.3324	1.6622	0.0017	0.171
	RMSE (μm)	0.0401	0.2007	0.0013	0.2939
Exp.	Phase lag (°)	-	-	0	0
	Maximum error (μm)	0.4000	2.5000	0.3000	1.1267
	RMSE(μm)	0.2238	0.7851	0.1355	0.4161

Sim.: simulation; Exp.: experiments.

3.3. The Combined Stage

We integrated the PZT and the motor stage with the control structure, as shown in Figure 9, where the PZT stage applies the multiple switching control with $(N = 3, H_P = 20, S_P = 2)$, while the motor stage employs the gain-scheduling control with command feedforward. The response predictor also applies a similar layout to estimate the stage responses by all possible control sequences. The predictor then calculates the corresponding system costs and selects the optimal control sequence for the PZT stage.
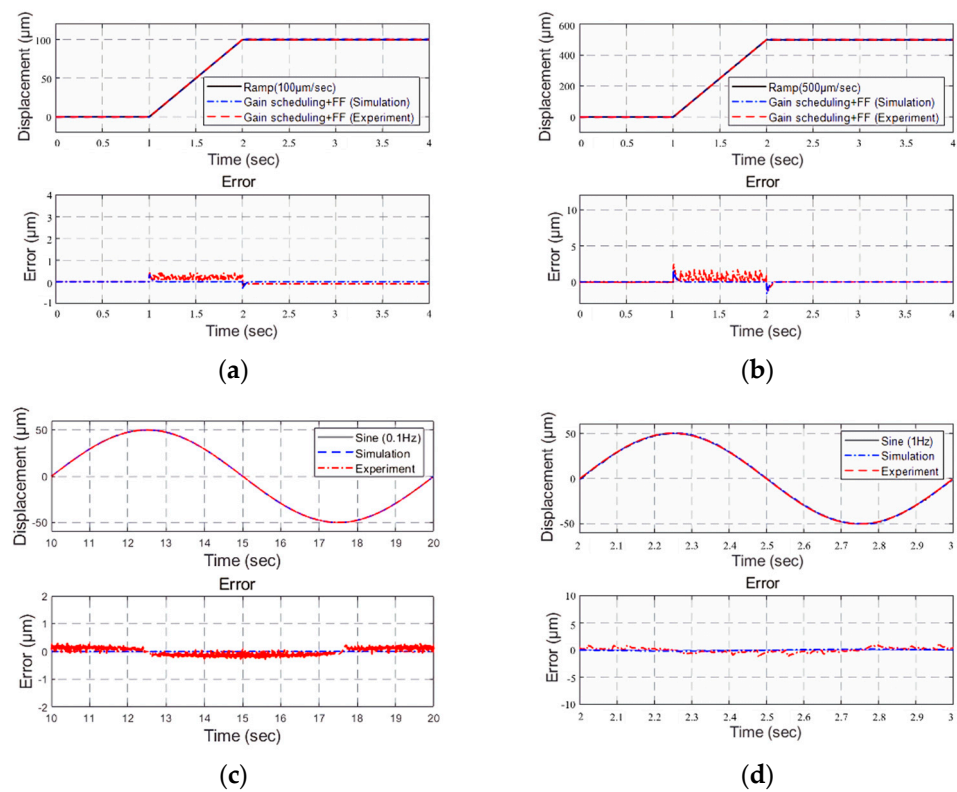
Figure 8. Tracking responses of the motor stage: (**a**) ramp input (100 μm/s); (**b**) ramp input (500 μm/s); (**c**) sinusoidal input (0.1 Hz); (**d**) sinusoidal input (0.1 Hz).
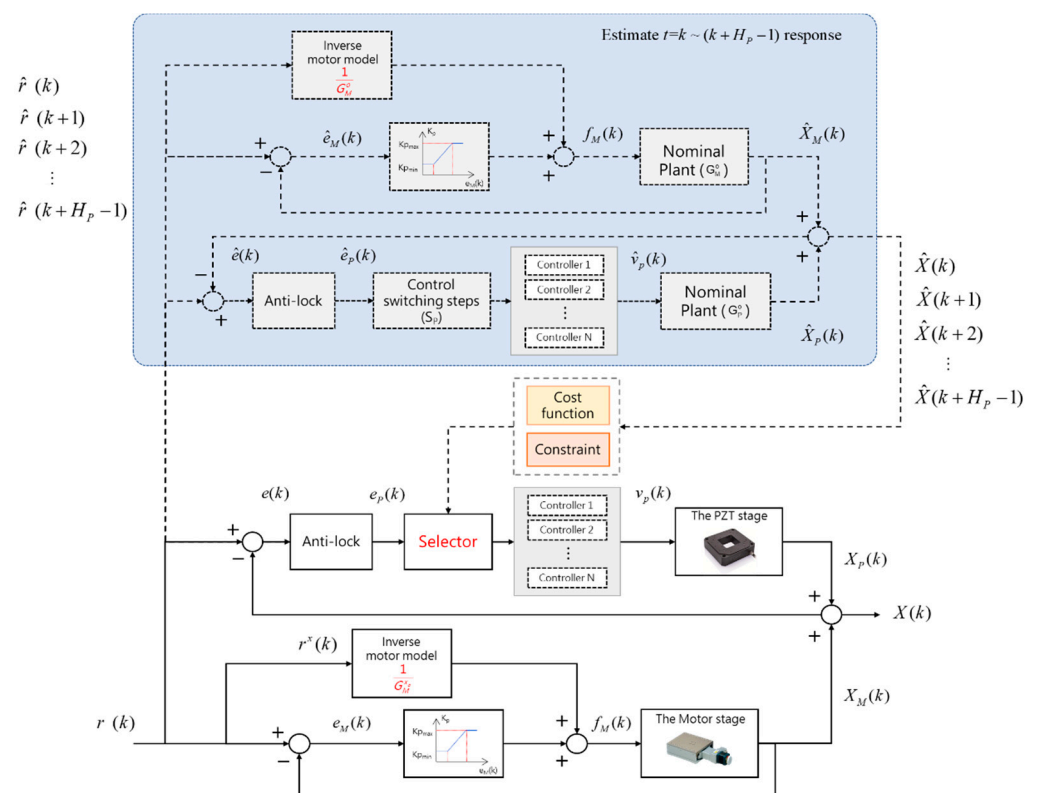

Figure 9. The switching control structure for the combined stage.

The motor stage applies gain-scheduling control based on the current positioning error $e_M(k) = r(k) - X_M(k)$, where $r(k)$ is the command and $X_M(k)$ is the motor stage position. Considering that the PZT stage has a travel limit of 50 μm, we set the following anti-lock function:

$$e_P(k) = \begin{cases} 0, & \text{if } |e(k)| \geq 50 \text{ μm} \\ r(k) - y_M(k) - y_P(k), & \text{if } |e(k)| < 50 \text{ μm} \end{cases} \tag{10}$$

where $e_P(k)$ is the error of the PZT stage and $e(k) = r(k) - X_M(k) - X_P(k)$ is the error of the combined stage. The PZT stage provides precision positioning using multiple switching control to regulate the position errors of the combined stage. Because the optimal parameters for the PZT stage are $N = 3$ and $S_p = 2$, the predictor estimates the system responses and calculates the corresponding system costs with all nine ($N^{S_P} = 9$) possible control sequences; it then chooses the optimal one to regulate the PZT stage.

For experimental verification, we applied the combined stage to track the word "NTU" with a scale of 100 mm × 50 mm, as shown in Figure 10a. The experimental results are illustrated in Figure 10 and Table 4. Compared with previous works [8,9], the RMSE was reduced, because the multiple switching control can quickly adjust the tracking errors at the turning points, as shown in Figure 10c,d. For example, the switching mechanism switched the x-axis controller of the PZT stage from $\overline{C}_F$ to $\overline{C}_M$ at $t = 331.990$ s, and from $\overline{C}_M$ to $\overline{C}_S$ at $t = 332.060$ s. Finally, the intermediate controller $\overline{C}_M$ was chosen at $t = 332.080$ s to complete the turning. Similarly, the switching mechanism switched the controller from $\overline{C}_F$ to $\overline{C}_S$ at $t = 564.008$ s, from $\overline{C}_S$ to $\overline{C}_M$ at $t = 564.023$ s, and from $\overline{C}_M$ to $\overline{C}_S$ at $t = 564.033$ s to complete tracking the turning point. Compared with previous studies [8,9], parameter optimization of the switching control led to significantly improved system performance.
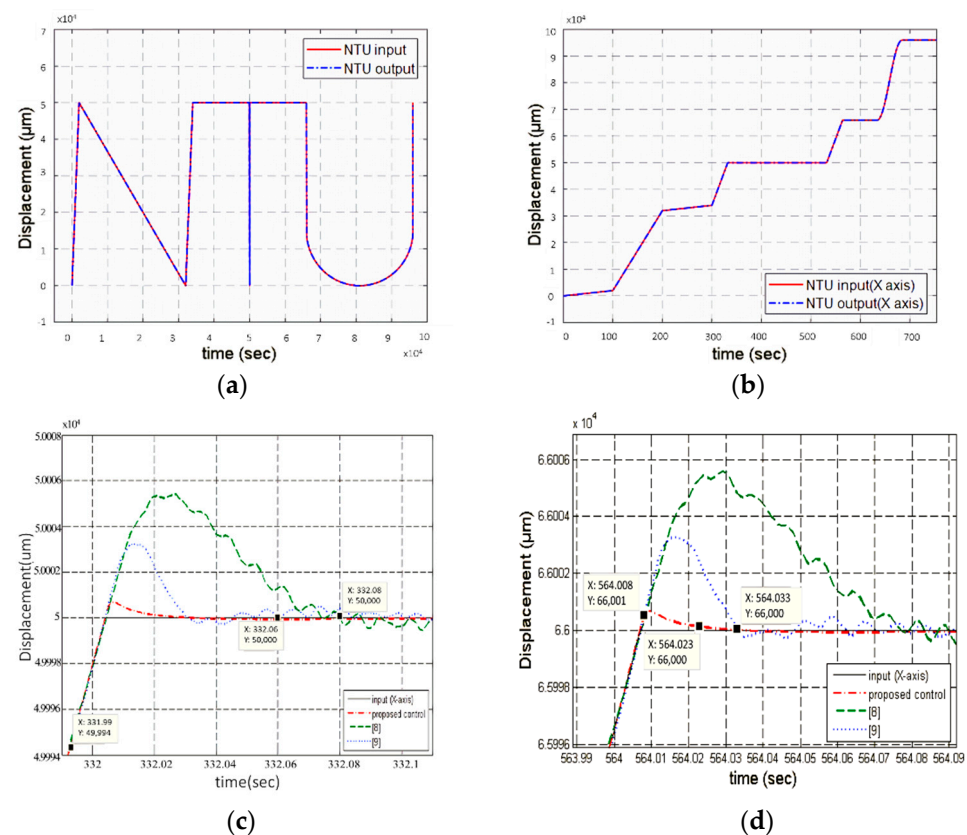

Figure 10. Experimental responses for tracking characters.: (**a**) character tracking; (**b**) x-axis responses; (**c**) zoom-in responses at the turning point around 332 s; (**d**) zoom-in responses at the turning point around 564 s.

Table 4. Tracking performance of the combined stage.

	RMSE
Control method in [8]	203.9 nm
Control method in [9]	140.5 nm
Multiple switching control	136.8 nm

### 3.4. Microfabrication by Two-Photon Polymerization

We integrated the combined stage with a TPP system, as shown in Figure 11 to fabricate a microlens. An adaptor with a microscope slide was connected to the PZT stage, and the laser was projected to fabricate microstructures by hardening the materials (OrmoComp) on the microscope slide. Note that the adaptor and the microscope slide were put on the stage when we identified the PZT stage models in Equation (2). Furthermore, the model variation caused by the loading effects can be neglected because the adaptor is lightweight. We demonstrate the effectiveness of the proposed control method using the images and optical properties of the microlens.
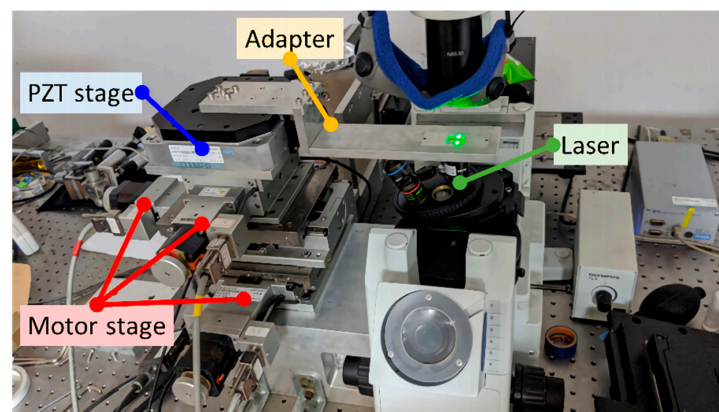
**Figure 11.** Integration of the combined stage and the TPP system.

The Fresnel zone plate (FZP) is a planar microlens designed to focus light. We designed an FZP with a diameter of 128 μm, as follows [28]:

$$r_n = \sqrt{nf\lambda + \frac{1}{4}n^2\lambda^2} \tag{11}$$

where n is the number of circles, r_n is the radius of the n-th circle, λ is the wavelength in μm, and f is the focal length of the lens in μm. For example, setting $n = 13$, $\lambda = 632.8$ nm, and $f = 500$ μm, the radius is calculated as $r_n = 18, 25, \cdots, 64$ μm when $n = 1, 2, \cdots, 13$. The design and fabrication results are shown in Figure 12.
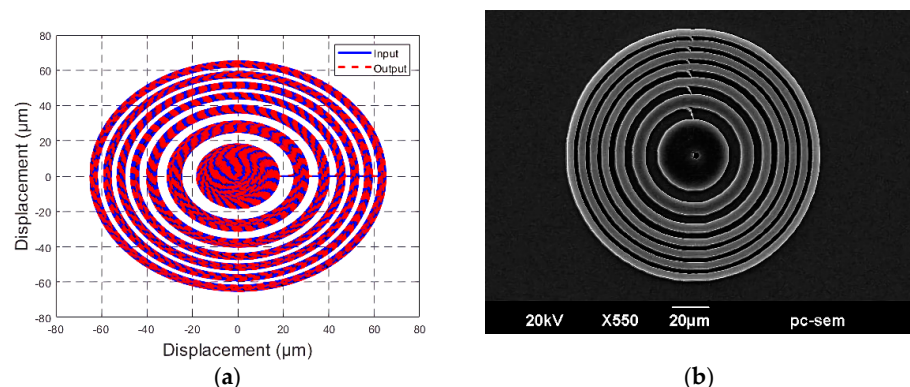
Figure 12. The design and fabrication of the FZP: (**a**) the lens design; (**b**) lens fabrication.

We evaluated the optical quality of the FZP by the light intensity and sharpness detected on the CMOS images. The FZP focused light onto a CMOS camera, as shown in Figure 13a, where the CMOS image was gray, scaled as black and white. Every pixel had a value of 0–255 to represent its brightness, as shown in Figure 13b, where 0 and 255 represented an image that was completely black and completely white, respectively. We analyzed the intensity of the image brightness along the red line, as shown in Figure 13c. The light sharpness was defined as the derivative of the intensity, as illustrated in Figure 13d. The tracking RMSE of the combined stage and the optical properties of the microlens are shown in Table 5. Compared with previous reports [8,9], the optical qualities of the microlens were greatly improved. The proposed multiple switching control employing iterative parameter tuning is therefore deemed effective in improving microfabrication.
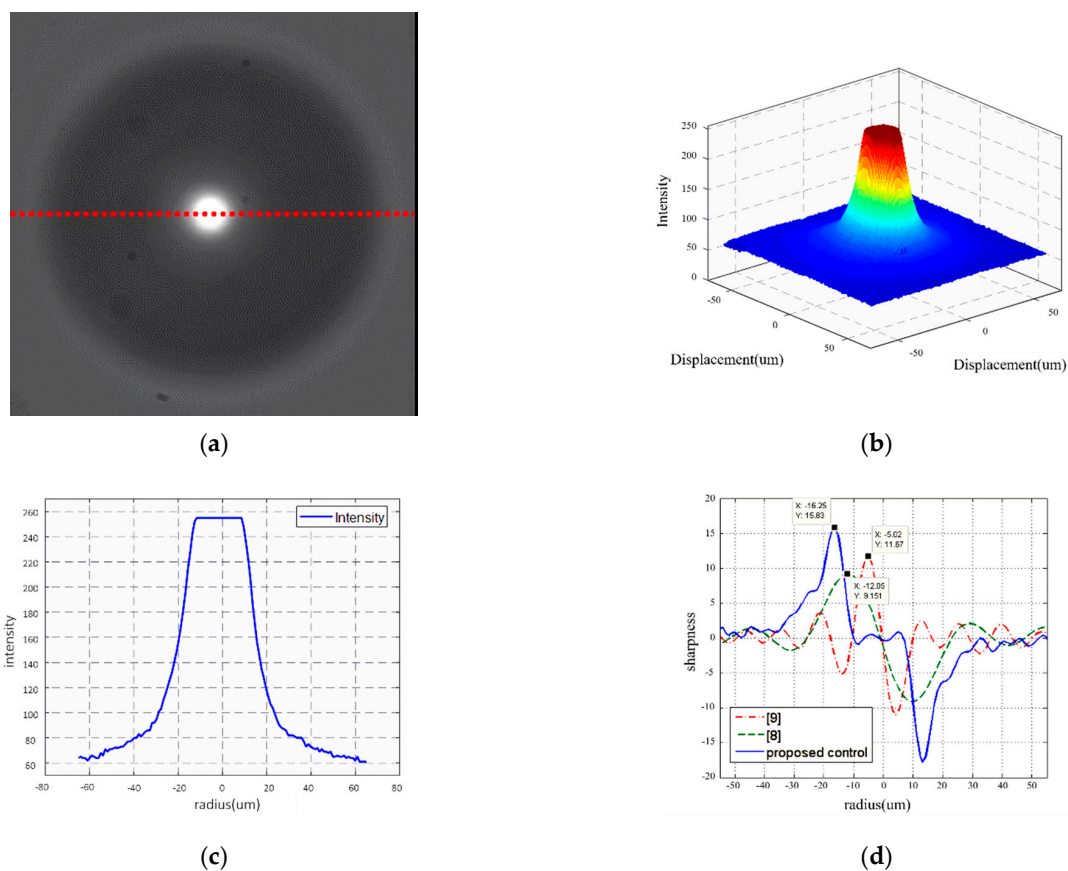
Figure 13. Optical properties of the micro-lens: (**a**) light spot; (**b**) brightness; (**c**) image intensity; (**d**) image sharpness.

Table 5. Comparison of the lens performance.

	Control in [8]	Control in [9]	Proposed Control
Intensity	164	255	255
Sharpness	9.15	11.7	15.8

4. Conclusions

This paper proposed an iteration procedure that optimizes the structure parameters for multiple switching control. Because control design is a compromise between various performance requirements, the merits of different controllers can potentially be achieved by switching them at appropriate moments. We introduced a multiple switching control structure and proposed an iteration method to optimize the structure parameters, such as the number of controllers and the prediction horizon. The iterative method began with a default set of parameters, which were iteratively tuned until they converged. We then

applied the proposed iterative optimization method to a long-stroke precision stage, and demonstrated its effectiveness via simulations and experiments. We further integrated the stage with a TPP system to fabricate a microlens and evaluate its optical properties. The results show that the proposed iterative method for multiple switching control is effective in improving the performance of microfabrication systems. The developed iteration parameter optimization method for multiple switching control is a general control technique, and can also be applied to other control systems—such as atomic force microscopes [29,30], air-bearing planar stages [31], and visual-servo systems [32]—to improve system performance.

Appendix A. Robust Control Design for the PZT Stage

We applied loop-shaping techniques (see Figure 2 of [10]), to design robust controllers for the PZT stage. The principles of loop shaping are:

1. Increasing the loop gains at low frequencies for disturbance rejection;
2. Decreasing the loop gains at high frequencies for noise attenuation;
3. Smoothing the magnitude slopes near the crossover frequency for stability consideration.

The weighting functions were iteratively adjusted and verified by the system performance by simulations and experiments. Finally, we selected the following weighting functions for the PZT stage:

$$W_F = \frac{50(s+40\pi)}{s(s+30\pi)}, \ W_M = \frac{20(s+15\pi)}{s(s+30\pi)}, \ W_S = \frac{15(s+10\pi)}{s(s+40\pi)}$$

where the subscripts F, M, and S represent fast, intermediate, and smooth, respectively. The corresponding robust controllers were designed as follows:

$$K_\infty^F = \frac{1.773s^5+792.5s^4+8.101s^3+2.597\cdot10^8s^2+2.464\cdot10^{10}s+5.213\cdot10^{11}}{s^5+874.1s^4+5.619\cdot10^5s^3+3.212\cdot10^8s^2+4.03\cdot10^{10}s+9.243\cdot10^{11}},$$

$$K_\infty^M = \frac{1.773s^5+792.5s^4+8.101s^3+2.597\cdot10^8s^2+2.464\cdot10^{10}s+5.213\cdot10^{11}}{s^5+874.1s^4+5.619\cdot10^5s^3+3.212\cdot10^8s^2+4.03\cdot10^{10}s+9.243\cdot10^{11}},$$

$$K_\infty^S = \frac{1.194s^5+466.6s^4+5.247\cdot10^5s^3+1.47\cdot10^8s^2+1.056\cdot10^{10}s+1.96\cdot10^{11}}{s^5+575.3s^4+4.67\cdot10^5s^3+1.964\cdot10^8s^2+1.333\cdot10^{10}s+2.341\cdot10^{11}}.$$

Then, the weighted controllers $C_F = W_F K_\infty^F$, $C_M = W_M K_\infty^M$, and $C_S = W_S K_\infty^S$ were implemented to the plant.

Appendix B. Robust PI Control Design by the PSO Algorithms

We applied PSO techniques to derive robust PI controllers, because the standard robust controllers are high-ordered, and might increase difficulties in implementation.

PSO is a stochastic optimization technique [27] that simulates the social behavior of birds and fish in order to effectively solve multidimensional optimization problems, especially for nonlinear systems. Figure A1 shows the concept of a particle swarm optimization algorithm, where X_i^k and V_i^k represent the particle's current velocity and position, respectively. Pbest$_i$ is the historical best position of the *i*-th particle, while Gbest is the best position among the swarms. Each particle updates its position and velocity through the following equations:

$$V_i^{k+1} = w \times V_i^k + c_1 \times \text{rand}_1 \times (\text{Pbest}_i - X_i) + c_2 \times \text{rand}_2 \times (\text{Gbest} - X_i),$$
$$X_i^{k+1} = X_i^k + V_i^{k+1}.$$

where w is the inertia weighting function for the velocity, c_1 and c_2 are learning factors, and rand$_1$ and rand$_2$ are random numbers between 0 and 1.
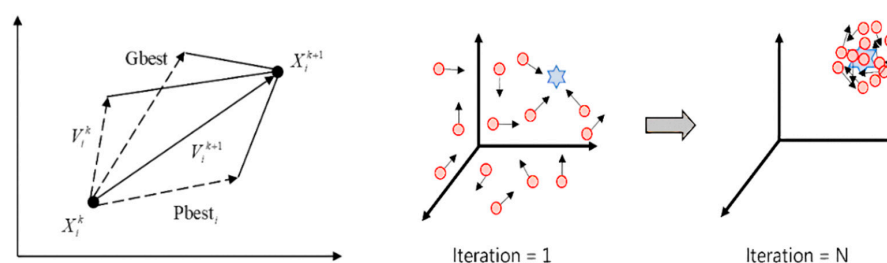

Figure A1. Particle swarm optimization.

We applied the PSO techniques to derive the following PI controllers:

$$C^{PI}(s) = K_P + \frac{K_I}{s}$$

which can provide similar responses to the standard robust controllers. We define the fitness function as follows:

$$F(K_P, K_I) = \sum_{i=1}^{n} \omega_i \cdot \overline{J}_i = \sum_{i=1}^{n} \omega_i \cdot \left(\frac{J_i^{PI}}{J_i^{Robust}} - 1 \right)^2$$

where J_i^{PI} and J_i^{Robust} represent the performance indices employing the PI and robust controllers, respectively. $\overline{J}_i$ indicates the similarity between the PI controller and the robust controller in terms of J_i, while ω_i represents the weighting of J_i. We set $n = 5$ and consider the following five indices:

1. Stability margin: $J_1 = b(G_P^0, C^{PI})$;
2. Root-mean-square error: $J_2 = \left(\left(\int_1^{1.2} |e(t)|_2 dt \right) / 0.2 \right)^{1/2}$;
3. Settling time: $J_3 =$ the settling time to a step input;
4. Overshoot: $J_4 =$ percentage overshoot of a step response;
5. Rising time: $J_5 =$ rising time to a step input.

We applied 100 particles with random initial values and set $w = 0.4$, $c_1 = 0.4$, $c_2 = 0.4$ with 50 iterations. The PSO algorithms iteratively update the parameters. Finally, the fast robust PI controller is designed as:

$$\overline{C}_F(s) = K_P^F + \frac{K_I^F}{s} = 0.05 + \frac{36.97}{s}$$

Similarly, the intermediate and the smooth PI controllers are derived as follows:

$$\overline{C}_M(s) = 0.08 + \frac{8.01}{s}, \ \overline{C}_S(s) = 0.05 + \frac{3.94}{s}$$

These controllers ($\overline{C}_F$, $\overline{C}_M$, and $\overline{C}_S$) are implemented for multiple switching control. We compare the system responses by these robust PI controllers with the standard robust controllers (C_F, C_M, and C_S), as illustrated in Table A1. First, all $\overline{J}_i \approx 0$ except for $\overline{J}_1$, indicating that the robust PI controllers provide similar time-domain characteristics to the higher-order robust controllers. Second, the robust PI controllers cannot achieve the original stability margins, because these robust controllers were designed to provide the maximum stability margins. However, system stability can still be guaranteed, because the stability margins of robust PI controllers are much larger than the system gap (0.0039).

Table A1. The performance costs for robust PI controller design.

		$\overline{J}_1$	$\overline{J}_2$	$\overline{J}_3$	$\overline{J}_4$	$\overline{J}_5$
C_F	$\overline{C}_F$	0.419	4.476×10^{-5}	2.100×10^{-2}	3.000×10^{-3}	5.100×10^{-5}
C_M	$\overline{C}_M$	0.520	4.300×10^{-3}	2.000×10^{-3}	5.371×10^{-5}	1.200×10^{-2}
C_S	$\overline{C}_S$	0.601	8.000×10^{-3}	6.573×10^{-4}	0	4.000×10^{-2}

Appendix C. Iterative Parameter Optimization for the PZT Stage

First, we set $(\ N,\ H_P,\ S_P\ ) = (\ 4,\ 40,\ 4\ )$ at step 1. At step 2, we apply $H_P = 40$ and $S_P = 4$ to optimize N; the results are shown in Figure A2a, where $J = 1.557$, 1.489, and 1.477 (µm) when N = 2, 3, and 4, respectively. Therefore, we set $N^{opt} = 3$, because it provides similar performance to N = 4, but with less computing load. At step 3, we apply $N^{opt} = 3$ and $S_P = 4$ to optimize H_P; the results are shown in Figure A2b, where J = 1.617, 1.489, and 1.489 (µm) when H_P = 5, 20, and 40, respectively. Hence, we set $H_P^{opt} = 20$, as this provides the best performance with a lesser prediction horizon. At step 4, we apply $N^{opt} = 3$ and $H_P^{opt} = 20$ to optimize S_P; the results are shown in Figure A2c, where J = 1.860, 1.489, and 1.489 (µm) when S_P = 1, 2, and 3, respectively. Therefore, we set $S_P^{opt} = 2$, because it provides the best performance with less computing load. At step 5, we notice that $\left(N^{opt} = 3,\ H_P^{opt} = 20,\ S_P^{opt} = 2\right) \neq (N = 4,\ H_P = 40,\ S_P = 4)$; therefore, we set $(N = 3,\ H_P = 20,\ S_P = 2)$ and return to step 1 to repeat the procedures. At the second iteration, the optimal parameters are found to be $\left(N^{opt} = 3,\ H_P^{opt} = 20,\ S_P^{opt} = 2\right)$, which is the same as $(N = 3,\ H_P = 20,\ S_P = 2)$, as illustrated in Table A2.
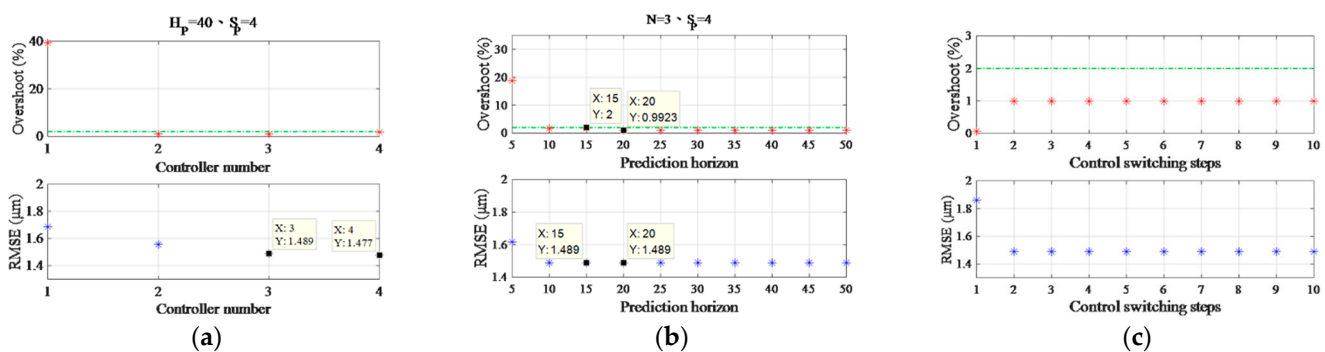
Figure A2. Iterative parameter tuning: (**a**) N optimization; (**b**) HP optimization; (**c**) SP optimization.

Table A2. Iterative parameter tuning for the PZT stage.

	Initial Setting Parameters	Optimal Parameters	Costs
Fitst iteration	$H_P = 40$, $S_P = 4$	$N^{opt} = 3$	$N = 2$, $J = 1.557$ μm $N = 3$, $J = 1.489$ μm $N = 4$, $J = 1.477$ μm
	$S_P = 4$, $N^{opt} = 3$	$H_P^{opt} = 20$	$H_p = 5$, J $= 1.617$ μm $N = 20$, $J = 1.489$ μm $H_p = 40$, $J = 1.489$ μm
	$N^{opt} = 3$, $H_P^{opt} = 20$	$S_P^{opt} = 2$	$S_p = 1$, $J = 1.860$ μm $S_p = 2$, $J = 1.489$ μm $S_p = 3$, $J = 1.489$ μm
Second iteration	$H_P = 20$, $S_P = 2$	$N^{opt} = 3$	$N = 2$, $J = 1.557$ μm $N = 3$, $J = 1.489$ μm $N = 4$, $J = 1.477$ μm
	$S_P = 2$, $N^{opt} = 3$	$H_P^{opt} = 20$	$H_p = 5$, J $= 1.617$ μm $H_p = 20$, $J = 1.489$ μm $H_p = 40$, $J = 1.489$ μm
	$N^{opt} = 3$, $H_P^{opt} = 20$	$S_P^{opt} = 2$	$S_p = 1$, $J = 1.860$ μm $S_p = 2$, $J = 1.489$ μm $S_p = 3$, $J = 1.489$ μm

References

1. Solihin, M.I.; Wahyudi; Legowo, A. Fuzzy-tuned PID anti-swing control of automatic gantry crane. *J. Vib. Control* **2010**, *16*, 127–145. [CrossRef]
2. Bashash, S.; Saeidpourazar, R.; Jalili, N. Tracking control of time-varying discontinuous trajectories with application to probe-based imaging and nanopositioning. In Proceedings of the 2009 American Control Conference, St. Louis, MO, USA, 10–12 June 2009.
3. Qin, Y.; Sun, L.; Hua, Q.; Liu, P. A fuzzy adaptive PID controller design for fuel cell power plant. *Sustainability* **2018**, *10*, 2438. [CrossRef]
4. Xu, S.; Wang, X.; Yang, J.; Wang, L. A fuzzy rule-based PID controller for dynamic positioning of vessels in variable environmental disturbances. *J. Mar. Sci. Technol.* **2019**, *25*, 1–11. [CrossRef]
5. Armaghan, S.; Moridi, A.; Sedigh, A.K. Design of a switching PID controller for a magnetically actuated mass spring damper. In Proceedings of the World Congress on Engineering, London, UK, 6–8 June 2011; Volume III.
6. Asl, R.M.; Mahdoudi, A.; Pourabdollah, E.; Klančar, G. Combined PID and LQR controller using optimized fuzzy rules. *Soft Comput.* **2019**, *23*, 5143–5155.
7. Rana, M.; Pota, H.R.; Petersen, I.R. MPC in high-speed atomic force microscopy. In Proceedings of the 2016 Australian Control Conference (AuCC), Newcastle, NSW, Australia, 3–4 November 2016.
8. Wang, K.-A.; Peng, Y.-K.; Wang, F.-C. The Development and Control of a Long-Stroke Precision Stage. *Smart Sci.* **2017**, *5*, 85–93. [CrossRef]
9. Wang, F.-C.; Peng, Y.-K.; Lu, J.-F.; Chung, T.-T.; Yen, J.-Y. Micro-lens fabrication by a long-stroke precision stage with switching control based on model response prediction. *Microsyst. Technol.* **2019**, *3*, 1–14. [CrossRef]
10. Wang, F.-C.; Lu, J.-F.; Su, W.-J.; Yen, J.-Y. Precision positioning control of a long-stroke stage employing multiple switching control. *Microsyst. Technol.* **2020**, *1*, 1–14. [CrossRef]
11. Nichols, R.A.; Reichert, R.T.; Rugh, W.J. Gain scheduling for H-infinity controllers: A flight control example. *IEEE Trans. Control. Syst. Technol.* **1993**, *1*, 69–79. [CrossRef]
12. Yamaguchi, T.; Shishida, K.; Tohyama, S.; Hirai, H. Mode switching control design with initial value compensation and its application to head positioning control on magnetic disk drives. *IEEE Trans. Ind. Electron.* **1996**, *43*, 65–73. [CrossRef]
13. Hossain, A.; Rahman, M. Comparative Analysis among Single-Stage, Dual-Stage, and Triple-Stage Actuator Systems Applied to a Hard Disk Drive Servo System. *Actuators* **2019**, *8*, 65. [CrossRef]
14. Zhu, W.; Rui, X.-T. Hysteresis modeling and displacement control of piezoelectric actuators with the frequency-dependent behavior using a generalized Bouc–Wen model. *Precis. Eng.* **2016**, *43*, 299–307. [CrossRef]
15. Saleem, A.; Al-Ratrout, S.; Mesbah, M. A fitness function for parameters identification of Bouc-Wen hysteresis model for piezoelectric actuators. In Proceedings of the 5th International Conference on Electrical and Electronic Engineering (ICEEE), Istanbul, Turkey, 3–5 May 2018.
16. Gan, J.; Zhang, X. Nonlinear hysteresis modeling of piezoelectric actuators using a generalized Bouc–Wen model. *Micromachines* **2019**, *10*, 183. [CrossRef]

17. Fang, J.; Wang, J.; Li, C.; Zhong, W.; Long, Z. A compound control based on the piezo-actuated stage with bouc–wen model. *Micromachines* **2019**, *10*, 861. [CrossRef]

18. Zhang, F.; Liu, J.; Tian, J. Analysis of the Vibration Suppression of Double-Beam System via Nonlinear Switching Piezoelectric Network. *Machines* **2021**, *9*, 115. [CrossRef]

19. Physik Instrumente P-517 ● P-527 Multi-Axis Piezo Scanner. Available online: https://www.physikinstrumente.com/en/products/nanopositioning-piezo-flexure-stages/multi-axis-piezo-flexure-stages/p-517-p-527-multi-axis-piezo-scanner-201500/ (accessed on 4 July 2021).

20. Piezomechanik Amplifier SVR/150/3. Available online: https://www.piezomechanik.com/products/ (accessed on 4 July 2021).

21. Chuo Precision Industrial Stepper Motor ALS-510-H1P. Available online: https://www.chuo.co.jp/contents/hp0543/list.php?CNo=543&ProCon=7065 (accessed on 4 July 2021).

22. Chuo Precision Industrial Stepper Motor ALV-104-HP. Available online: https://www.chuo.co.jp/contents/hp0058/list.php?CNo=58&ProCon=94 (accessed on 4 July 2021).

23. National Instruments DAQ Card PCI-6221 and PCI-6229. Available online: https://www.ni.com/zh-tw.html (accessed on 4 July 2021).

24. Glover, K.; McFarlane, D. Robust stabilization of normalized coprime 457 factor plant descriptions with H/sub infinity/-bounded uncertainty. *IEEE 458 Trans. Autom. Control* **1989**, *34*, 821–830. [CrossRef]

25. Georgiou, T.T.; Smith, M.C. Optimal robustness in the gap metric. In Proceedings of the 28th IEEE Conference on Decision and Control, Tampa, FL, USA, 13–15 December 1989.

26. McFarlane, D.; Glover, K. A loop-shaping design procedure using H/sub infinity/synthesis. *IEEE Trans. Autom. Control* **1992**, *37*, 759–769. [CrossRef]

27. Kennedy, J.; Eberhart, R. Particle swarm optimization. In Proceedings of the ICNN'95-International Conference on Neural Networks, Perth, WA, Australia, 27 November–1 December 1995.

28. Meyrán, G.J. Augustin-Jean Fresnel. *Rev. Mex. Oftalmol.* **2008**, *2*, 82.

29. Zhang, Y.; Fang, Y.; Zhou, X.; Dong, X. Image-based hysteresis modeling and compensation for an AFM piezo-scanner. *Asian J. Control* **2009**, *11*, 166–174. [CrossRef]

30. Lu, H.; Fang, Y.; Ren, X.; Zhang, X. Improved direct inverse tracking control of a piezoelectric tube scanner for high-speed AFM imaging. *Mechatronics* **2015**, *31*, 189–195. [CrossRef]

31. Kuo, F.-C.; Hsu, C.; Hsieh, M.-R.; Yen, J.-Y.; Chen, L.-C.; Chung, T.-T.; Wang, F.-C. Study on the transient response to the point-to-point motion controls on a dual-axes air-bearing planar stage. *Int. J. Adv. Manuf. Technol.* **2020**, *111*, 2759–2772. [CrossRef]

32. Liu, L.-C.; Yang, P.-H.; Liao, S.-C.; Li, B.-P.; Wang, F.-C.; Lin, P.-C. Development of a dual-stage and visual-servo filming robot. *Proc. Inst. Mech. Eng. Part I J. Syst. Control Eng.* **2021**, *235*, 0959651821991363.